scientific reports

OPEN

Photocatalytic and antibacterial activity properties of Ti surface treated by femtosecond laser–a prospective solution to peri-implant disease

Adriana Barylyak[1]✉, Renata Wojnarowska-Nowak[2], Małgorzata Kus-Liśkiewicz[3], Piotr Krzemiński[4], Dariusz Płoch[2], Bogumił Cieniek[2], Yaroslav Bobitski[4,5] & Joanna Kisała[6]✉

Laser texturing seems to be a promising technique for reducing bacterial adhesion on titanium implant surfaces. This work aims to demonstrate the possibility of obtaining a functionally orientated surface of titanium implant elements with a specific architecture with specific bacteriological and photocatalytic properties. Femtosecond laser-generated surface structures, such as laser-induced periodic surface structures (LIPSS, wrinkles), grooves, and spikes on titanium, have been characterised by XRD, Raman spectroscopy, and scanning electron microscopy (SEM). The photocatalytic activity of the titanium surfaces produced was tested based on the degradation effect of methylene blue (MB). The correlation between the photocatalytic activity of TiO_2 coatings and their morphology and structure has been analysed. Features related to the size, shape, and distribution of the roughness patterns were found to influence the adhesion of the bacterial strain on different surfaces. On the laser-structurised surface, the adhesion of *Escherichia coli* bacteria were reduced by 80% compared to an untreated reference surface.

Keywords Micro/nano-structured surface, Reduced bacterial adhesion, Ultra-short pulsed laser treatment, Photocatalytic activity

In the arsenal of modern dentistry today there is a wide range of available implants, among which titanium and its alloys predominate due to their resistance to body fluid effects, high corrosion resistance, high tensile strength, flexibility, and biocompatibility[1,2]. Dental implants require compatibility with hard tissues for bone formation and bonding to the bone, compatibility with soft tissues for gingival epithelial adhesion, and antimicrobial properties to prevent bacterial invasion. Surface treatment is a process that changes the morphology, structure, and composition or function of the surface while leaving the mechanical properties of the bulk material. Since the first clinical applications, modifications of such surfaces have been widely studied to improve the osseointegration process[3]. Implantable devices used in dental rehabilitation typically consist of three parts: a bone-anchored implant, a connecting platform that transitions from the hard tissue to the soft tissue complex, and a prosthetic tooth[4]. Furthermore, the clinical success of implantation depends largely on ensuring that trans-mucosal platforms, which rely on the firm attachment of the gingiva to the implant abutment, do not allow oral bacteria to reach the bone-integrated surface. It is well known that the main problem in this transition area is bacterial colonisation and the development of inflammation around the implant[5,6]. Scientists describe this phenomenon as competition for substrate colonisation in the first stages of bio-integration[7]. This competition on dental implants occurs between hard and soft tissue cells, as well as bacterial cells. An ongoing question is what types of surface treatments can be useful to improve the adhesion of soft tissues and enhance the antibacterial properties in this

[1]Danylo Halytsky Lviv National Medical University, Pekarska Str. 69, Lviv 79010, Ukraine. [2]Institute of Materials Engineering, University of Rzeszow, Pigonia 1 Str., 35-959 Rzeszow, Poland. [3]Institute of Biotechnology, University of Rzeszow, Pigonia 1 St, 35-310 Rzeszow, Poland. [4]Institute of Physics, University of Rzeszow, 35-959 Rzeszow, Poland. [5]NoviNano Lab LLC, Pasternaka 5, Lviv 79015, Ukraine. [6]Institute of Biology, University of Rzeszow, Zelwerowicza 4 Str., 35-601 Rzeszow, Poland. ✉email: adriana.barylyak5@gmail.com; jkisala@ur.edu.pl

area. It has been shown that higher values of roughness parameters increase the number of colonies attached to the surface compared to smooth surfaces, regardless of the substrate material[8,9]. Basic and preclinical research shows that nano-topographies, biomimetic coatings and antibiotic release properties can modulate, align, and direct the growth of cells and soft tissues and reduce biofilm formation[10]. A promising prospect is implant surfaces with a micro/nano-structure, as opposed to smooth surfaces in contact with soft tissues, characterised by antibacterial and photocatalytic properties.

The modern concept of processing implanted surfaces is associated with the creation of the entire surface with identical morphology[11]. With the development of nanotechnology, it is possible to create nano-topographies with various controlled surface properties and modulate the osteoimmune response[12,13]. The possibility of designing surfaces with selective and morphologically standardised features using innovative laser technologies aimed at achieving the desired effect (osteointegration, biocompatibility, or antibacterial properties) seems promising[14,15]. We can call such surfaces "oriented" towards the expected therapeutic effect. The versatility and variability of laser processing of a real surface in the femtosecond pulse mode with obtaining unique architectonics are shown in the published works[16–18]. Changes in roughness, surface free energy, chemical composition, and nanostructure formation directly affect bacterial adhesion to the implant surface[19–21]. Several studies demonstrate the antimicrobial potential of laser-treated surfaces[21,22] because of the ability of the laser to alter surface properties such as wettability, roughness, morphology, and chemical composition and to create surfaces with different types of nano- and micro-textures to which bacteria are sensitive[19,22–25]. The surface pattern would determine the contact area and the adhesion force of the bacteria to the surface. The surface properties steer immunomodulatory processes, facilitating osseointegration, and promoting antibacterial efficacy.

Surface texturing by ultrafast laser direct writing methods differ from other surface modification methods due to their flexibility, simplicity, and high reproducibility in the fabrication of different types of nano- and microtextures[26]. Moreover, the laser treatment does not lead to material surface contamination, and lasers allow texturing large areas of parts with complex geometry, such as dental and orthopedic implants. Techniques commonly used to create surface textures in commercial applications are mechanical (machining, sandblasting) or chemical methods (such as acid etching and oxidation)[27]. Laser texturing, unlike the methods mentioned above, provides a high-quality surface with the desired properties in a one-step process (at the same time, we can modify the surface morphology and chemical composition).

The aim of this work is to demonstrate the possibility of obtaining a functionally oriented surface of titanium implant elements with a specific architecture and specific bacteriological and photocatalytic properties.

Materials and methods

Materials

The material investigated in this study was the grade 4 titanium disc samples (the most commonly used grade of titanium to produce dental implants) 4 ASTM B348 EN10204/3.1. The remaining reagents were analytical grade and were used as received.

Surface preparation

The titanium rod was cut into pieces (14 mm diameter and 5 mm high) and their surface was sandblasted with Al_2O_3 with a particle size of 53–75 µm under a pressure of 4 atmospheres and then polished to a mirror quality to obtain flat surfaces for laser processing. The structure generation was carried out using a Pharos P-20 femtosecond laser system that provides femtosecond pulses ($\tau = 213$ fs) at a central wavelength of 1030 nm with a spectral width of 15 nm, $M2 \simeq 1.1$. The laser beam was focused on the titanium surface at a spot diameter of 10.4 µm (at level 1/e2). A scanning mode with various overlaps was used for irradiation. Laser parameters have been summarised in Table 1.

Morphological and structural surfaces characterisation

Field emission scanning electron microscope (FESEM) Helios NanoLab 650 (FEI, Hillsboro, Oregon, USA) operating at 5 kV and 18 kV using an ETD detector with secondary electron (SE) imaging mode was used to obtain the images of morphology of prepared surfaces. Analysis was carried out over the entire sample area. XRD patterns were recorded with an X-ray diffractometer (D8 Advance, Bruker, Germany) and 0.15406 nm Cu K_α radiation. The surface roughness was measured by confocal laser microscope Olympus OLS5100 LEXT 3D (Olympus Co., Tokio, Japan). The Raman spectra were obtained using an inVia Micro Raman Renishaw spectrometer (Renishaw, Wotton under Edge, Gloucestershire, UK) combined with a Leica DM 2500 M microscope

Sample	Energy per pulse, Ep (mJ)	Pulse frequency, (kHz)	Peak fluence, (J/cm^2)	Step, (µm)	Polarisation	Scanning speed, V_s (m/s)
A_1	8	500	3.28	5	⊥	0.2
A_2	4	1000	1.64	10	⊥	0.8
A_3	1.95	1000	0.8	5	⊥	1
A_4	0	0	0	0	–	0

Table 1. Laser process parameters.

(Leica Microsystems GmbH, Wetzlar, Germany) equipped with a 488 nm and 633 nm laser as an excitation source. Measurements were taken with a spot metering mode and a map mode.

The water wetting angle of the sample was tested using a Nikon C-PS stereoscopic microscope with a camera from the Nikon MA-200 microscope and Nikon NIS software. Five microlitres of distilled water was dropped with a pipette. The result was given as the average of 5 measurements with standard deviation.

Surface photocatalytic properties

Photocatalytic properties were evaluated in the degradation reaction of methylene blue (MB). Titanium discs (A_1, A_2, A_3, or A_4) were placed in a quartz beaker, where MB solution was added (30 cm^3, 5×10^{-5} mol/dm^3, pH = 6). The MB solution without disc was irradiated parallelly to measure MB photolysis. The irradiation was performed with a handmade blue diode lamp as a light source (power density 8.78 W/m^2 measured by the Peak Tech 5025 digital lux meter, wavelength 455 nm) held at 30 cm from the sample. MB decay was monitored by spectrophotometric measurements (VWR UV–VIS 3100 PC spectrophotometer) at regular time intervals. External standards of five concentration ranged from 5×10^{-5} to 5×10^{-6} mol/dm^3.

Antibacterial tests

All reagents (chemical grade) were purchased from Sigma-Aldrich (U.S.A) or POCH (Poland) companies. Nutrient broth and agar (BTL, Poland) or phosphate buffered saline (Sigma-Aldrich, USA) were used for bacteria culture and serial dilutions, respectively. All assays were carried out in a laminar flow hood (Thermo Scientific, MSC Advantage). *Escherichia coli* PCM2209 was obtained from the Microbiological Collection deposited at the Institute of Biotechnology, University of Rzeszow, Poland. The overnight culture, incubated under aerobic conditions at 37 °C, was diluted to give an initial concentration of approximately 1×10^4 cells/mL and poured onto the titanium disc (sterilised prior to alcohol treatment). After 24 h of incubations, non-adhered bacteria were removed by aspiration of the medium followed by rinse with PBS. The discs were immersed with 5 mL of PBS and were sonicated in order to remove the bacteria adhered to the disc. Subsequently, serial dilution of the sample were plated onto the agar plates followed by overnight incubation at 37 °C. Colony forming unit (CFU) were calculated and the percentage of reduction (%R) in the growth of bacteria was estimated according to the formula:

$$\%R = \frac{CFUcontrol - CFUsample}{CFUcontrol} \times 100$$

In order to investigate the adhesion potential of bacteria depending on the surface structure, SEM images were recorded. Briefly, *E. coli* cells were seeded on the titanium disc and were incubated for 4 h. After the time, the disc was carefully rinsed to remove the unattached cells and the adherent cells were fixed in 2.5% glutaraldehyde for 60 min. After this, the discs were dehydrated in 30%, 50%, 70%, 85% and 95% ethanol for 5 min, respectively, and 100% ethanol for 20 min. The SEM analysis was carried out using a TLD electron detector in the secondary electron (SE), the samples were sputtered with a 4 nm gold layer.

Results and discussion

Morphological characterisation of surfaces

Based on microscopic observations (Fig. 1), an ordered structure of spikes can be observed for sample A_1. 'Spikes' are self-assembling structures that have a spherical shape on the micrometre scale, generated by ultrashort pulses polarised with energy per pulse well above the ablation threshold of the high repetition rate (to maintain the heat accumulation process). One can observe a pattern of grooves for A_2 sample. Laser Induced Periodic Surface Structures (LIPSS) are formed for sample A_3. LIPSS, also known as surface ripples or nano gratings, are parallel periodic grooves formed on the surface of materials due to laser irradiation[28]. They are usually perpendicular to the laser polarization have a period proportional to the laser's wavelength.

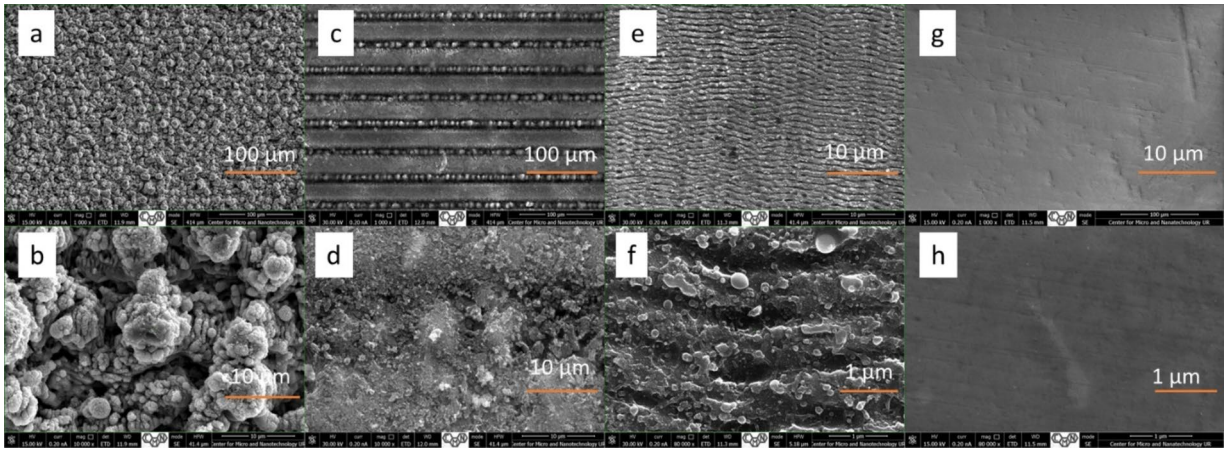

Figure 1. SEM images of structurised surfaces in different magnification of A_1 (**a**, **b**), A_2 (**c**, **d**), A_3 (**e**, **f**), A_4 (**g**, **h**).

Generally, laser-induced periodic surface structures (LIPSSs) are categorised on their spatial period. They are divided into two main types: low-spatial frequency LIPSS (LSFL) and high-spatial frequency LIPSS (HSFL). Low-spatial frequency LIPSS (LSFL) are characterised by periods larger than half of the laser irradiation wavelength, whereas high-spatial frequency LIPSS (HSFL) exhibit periods smaller than half of the incident wavelength[29]. HSFL aligned parallel to the laser beam polarisation is observed under low fluence conditions. Laser treatment using femtosecond pulses is a convenient technique for generating surface structures for various functional applications. Femtosecond laser texturing has proven to be ideal for producing structures with different dimensions and morphology (A_1—spikes, A_2—grooves, A_3—LIPSS) without additional processes.

A assessment of surface wettability was carried out by observing the behaviour of distilled water drops on the disc surface (Fig. 2). The shape of the drop on the all surfaces suggests its hydrophilic nature. It is confirmed by the contact angle values for samples, which are 16.8 ± 1.8 (A_1), 44.1 ± 3.3 (A_2), 52.5 ± 7.5 (A_3) and 56.0 ± 1.4 (A_4). The samples with smooth surface have larger contact angle than samples with a distinct texture. SEM images suggest that the surfaces of the samples differ significantly in roughness. Roughness, in a sense, affects the wettability of a solid. The reduction in wetting associated with roughness is important for the design of a super-hydrophobic surface. Super-hydrophobic surfaces have been gaining attention due to their self-cleaning and anti-adhesive properties. Several authors have reported a decrease in bacterial adhesion on such surfaces[30–33]. Surface roughness strongly influences the contact angle and wettability of the surface. The roughness effect depends on whether the droplet wets the surface grooves or whether air pockets remain between the droplet and the surface[34].

The analysed roughness parameters were: S_a—the arithmetical mean height; S_z—the average maximum height; S_p—the sum of the maximum peak height; S_{ku}—kurtosis; S_{dq}—the root mean square gradient; and S_{dr}—the developed interfacial area ratio (all values are in Table 2). The arithmetic mean height parameter (S_a) represents the arithmetic mean of the absolute height Z(x,y) within the evaluation area. The S_a values of the samples decreased in the following order: A_1 > A_2 > A_3 > A_4. This can be explained by the fact that the surface of sample A_1 has a spiky morphology, A_2 has a groove pattern, A_3 has a LIPSS structure (which is plain) on its surface, while sample A_4 has a flat surface because it has not been treated.

The average maximum height (S_z) parameter changes with the same trend as the S_a parameter. S_z is equivalent to the sum of the maximum peak height and maximum valley depth, so this parameter corresponds to the R_z parameter for line roughness. The value of the S_{ku} parameter (kurtosis) is a measure of the sharpness of the roughness profile. If $S_{ku} < 3$, the height distribution is asymmetric above the mean plane, whereas if $S_{ku} > 3$, the height distribution is peaked. Samples A_2, A_3, and A_4 have sharp distribution of hight, whereas the A_1 sample has even. The root mean square gradient (S_{dq}) is calculated as the root mean square of the slopes at all points in the defined area. The S_{dq} of a completely level surface is 0. When a surface has any slope, its S_{dq} value becomes larger. Sample A_1 presented the highest local steepness of the surface, A_2 had a moderate slope, while the surfaces of samples A_3 and A_4 were almost flat (Fig. 3).

The developed interfacial area ratio parameter (S_{dr}) signifies the rate of increase in the surface area. The increase rate is calculated from Eq. (1):

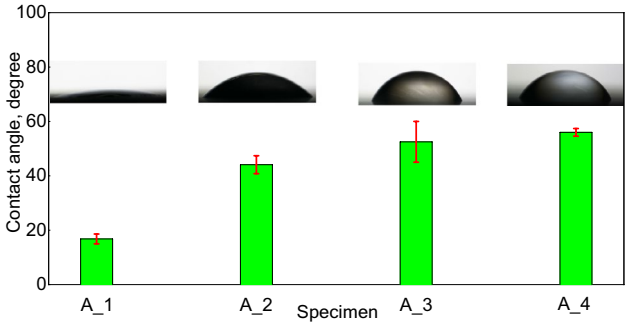

Figure 2. The water wetting angle of the surfaces.

	S_z* [µm]	S_a* [µm]	S_{ku}*	S_{dq}*	S_{dr}* [%]
A_1	26.885	3.280	2.364	3.973	169.779
A_2	12.384	0.983	3.554	0.782	21.742
A_3	3.295	0.171	3.713	0.298	4.180
A_4	1.100	0.061	3.519	0.181	1.710

Table 2. Roughness parameters. *S_z—the average maximum height; S_a—the arithmetical mean height; S_{ku}—kurtosis; S_{dq}—the root mean square gradient; and S_{dr} – the developed interfacial area ratio.

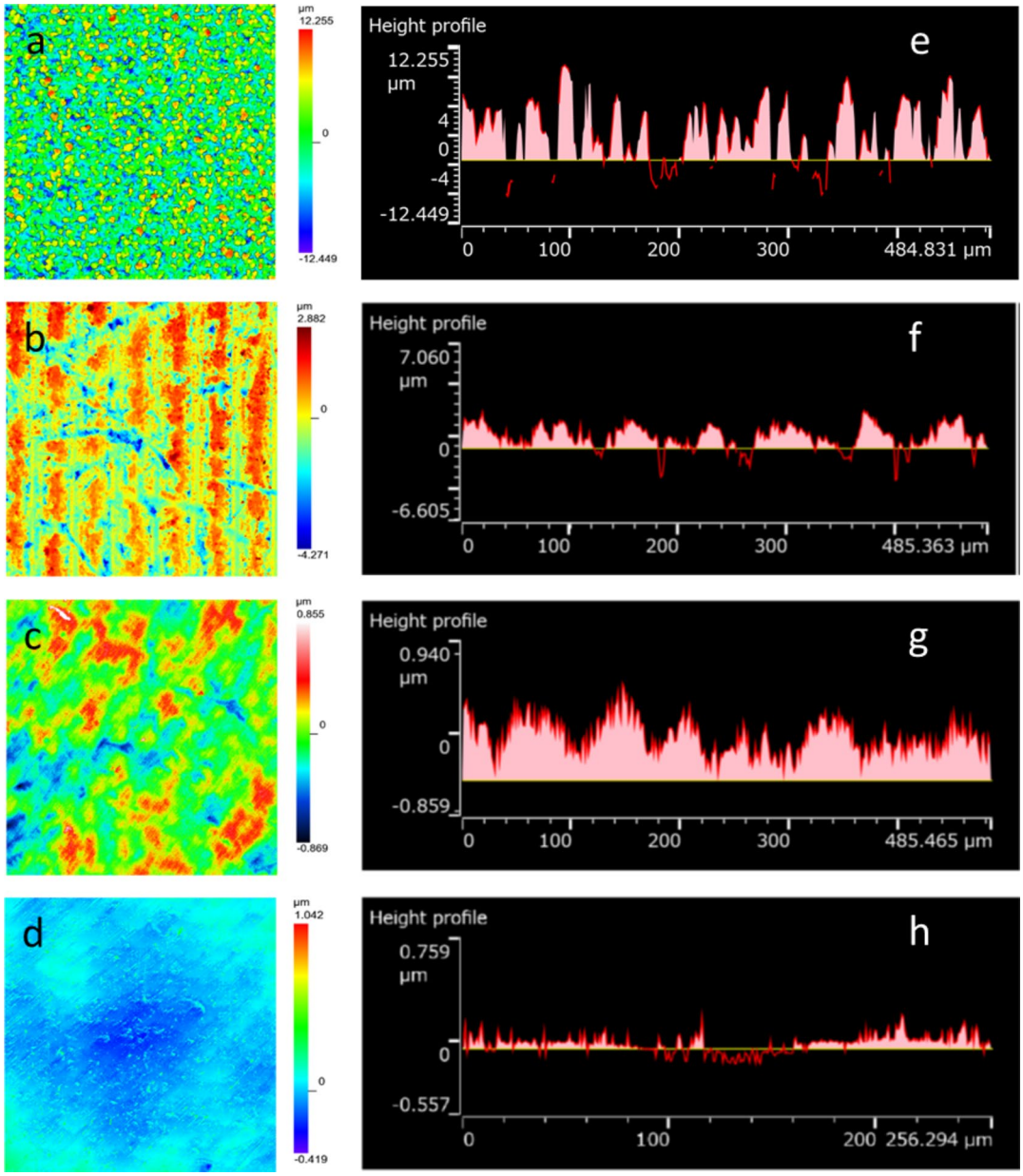

Figure 3. Roughness characterisation: 3D (areal) roughness presentation for A_1 (**a**), A_2 (**b**), A_3 (**c**), and A_4 (**d**); 2D roughness profiles of samples A_1 (**e**), A_2 (**f**), A_3 (**g**), and A_4 (**h**).

$$S_{dr} = \left\{ \left(\frac{A_1}{A_0} \right) - 1 \right\} \cdot 100\% \tag{1}$$

where A_1—surface area of the scale-limited surface; A_0—projected area.

The highest S_{dr} parameter has been measured for the A_1 sample, for the A_2 sample the moderate value, and the lowest for A_3 and A_4. These results mean that the sample A_1 surface is the roughest. Surface roughness is a predisposing factor to cellular adherence[35–37]. A positive relationship has been found between bone-to-implant contact and implant surface roughness by Shalabi et al.[38] Nano-roughness is considered to be the closest to natural tissue morphology, and it is an ideal factor that has a positive effect on cell adhesion, growth, and maturation. For example, in human venous endothelial cells, increasing the surface of the roughness of the biomaterial at the nanometric scale can enhance cell adhesion and growth on the rough surface[39]. Structural characterisation of surfaces.

The crystal phases were analysed using an X-ray diffractometer (XRD; D8 Advance, Bruker, Ettlingen, Germany) with Cu K_α ($\alpha = 0.154056$ nm) radiation, operated at 40 kV and 36 mA. In order to identify the chemical/structural composition of the oxide that is present at the surface of the structures, one useful technique is the X-ray diffraction (XRD). Since the Fig. 4A shows the XRD measurements of a polished titanium sample (A_4, non-irradiated sample, black line) as a reference and the measurements recorded for irradiated samples (A_1

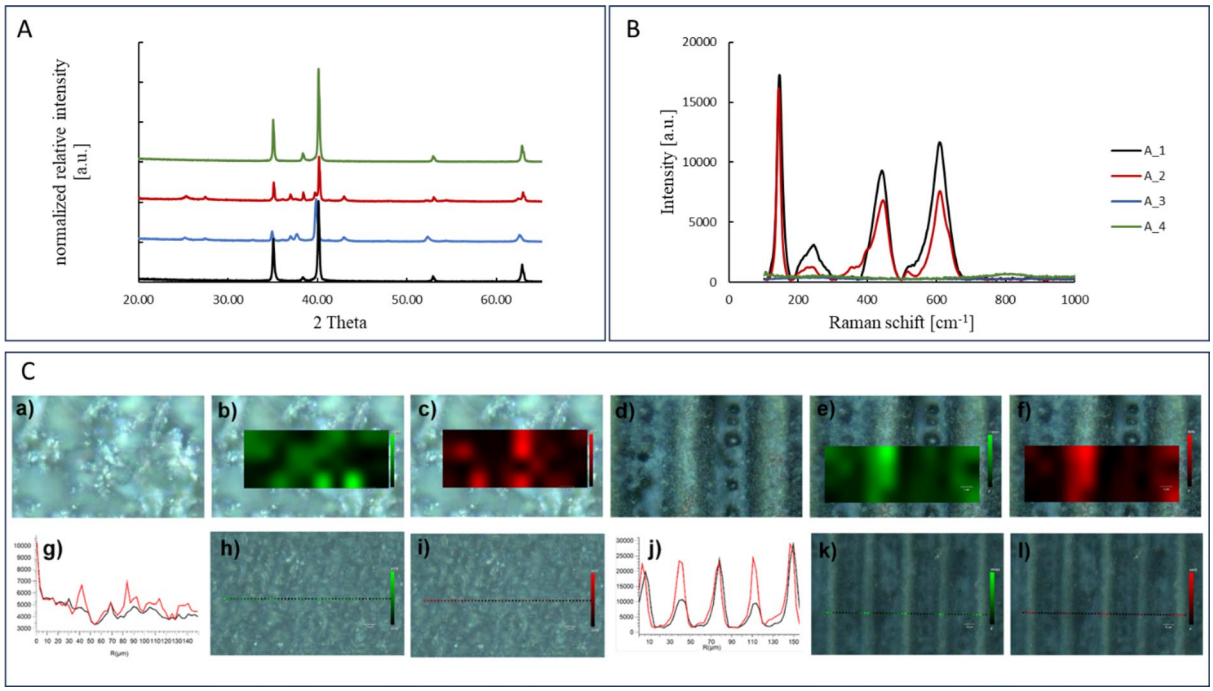

Figure 4. (**A**) XRD patterns of samples A_1 (blue), A_2 (red), A_3 (green), and A_4 (black); (**B**) Raman representative spectra of A_1 (black line). A_2 (red line). A_3 (blue line) and A_4 (green line) (**B**); (**C**) Raman map of the A_1 (a, b, c, g, h, i) and A_2 (d, e, f, j, k, l) sample with the surface morphology (a, d), marked the measurement position and lines intensity corresponding to anatase (b, e, h, k—green) and rutile ((c, f, i, l—red) form, graphical representation of anatase (green line) and rutile (red line) signal intensity (g, j) measured along the lines at images (h, i) and (k, l), respectively.

blue line, A_2 red line, and A_3 green line). The observed XRD reflexes can be assigned to Ti (reflexes at 35, 38, 40 and 52.5°2Θ) and TiO_2 (25, 27.5, 36, 42°2Θ) (Fig. 4A).

Reflections from other components were not observed. Reflex assignation was carried out with the ICDD PDF database[40] and crystallographic open database COD[41].

The samples (A_1. A_2. A_3. and A_4) were analysed by Raman spectroscopy to determine the composition of the surface layer. especially the presence of the titanium oxides or other oxides. The results obtained showed the presence of titanium oxides on the surface of samples A_1 and A_2. It was not observed in samples A_3 and A_4. The spectra collected on the tested samples are compared in the Fig. 4B.

The recorded Raman spectra of the A_1 and A_2 samples contain several bands characteristic for the TiO_2 material in anatase and rutile orthorhombic crystal systems. Anatase has Raman active vibrational modes at 146/cm (E_g). 329/cm (week line). 394/cm (B_{1g}). 517/cm (A_{1g}). and 636/cm (E_g) which have been observed. The active vibrational modes assigned to the rutile form have appeared. Rutile has the Raman active vibrational modes at 141/cm (B_{1g}), 244/cm (E_g). 442/cm (E_g) and 610/cm (A_{1g})[42–44]. Table 3 shows the exact position of the spectral bands and their identification.

Band position (/cm)	Band identification	Crystal structure
141	B_{1g}	Rutile
146	E_g	Anatase
244	E_g	Rutile
329	B_g	Anatase
357	A_g	Anatase, Rutile
394	B_{1g}	Anatase
442	E_g	Rutile
517	A_{1g}	Anatase
610	A_{1g}	Rutile
636	E_g	Anatase

Table 3. Frequency and identification of Raman bands of anatase and rutile structure[42–44].

The Raman spectra of A_1 and A_2 samples contained lines characteristic of rutile and anatase TiO_2 forms, but their intensity was different depending on the position on the sample.

The recorded spectrum maps show the distribution of titanium oxides on the surface of the samples, and they are presented in Fig. 4C. This distribution is random for A_1 sample, whereas for the A_2 sample it is very regular and repeatable. The arrangement of the titanium oxides is periodic. The prepared maps showed a higher concentration of the oxides on hills and smaller in the valleys, which was determined by analysing the intensity of the Raman bands. This is true for both the anatase and rutile forms.

Semiquantitative analyses of phase content (rutile, anatase) on surfaces A_1 and A_2 were performed on the map with the dimension 45 µm × 15 µm. For calculation 40 spectres were used for one sample (4 rows, 10 spectra in a row, intervals between measurements 5 mm) according to Zanatta et al.[45] with further modifications by the Jasinski et al.[46] method. The %Rut values were obtained by taking into account the intensity (Int) of the bands assigned to rutile (Int R) determined by matching a mathematical function that fits the characteristic curves of this form and the intensity (Int) of the bands assigned to rutile to anatase (Int A) according to the Eq. (2):

$$\%\ \mathrm{Rut(Int)} = \frac{\mathrm{IntR}}{(\mathrm{IntR} + \mathrm{IntA})} \cdot 100\% \tag{2}$$

where IntR was calculated as band intensity at 442 and 610/cm, IntA was calculated form band intensity at 394, 517, and 636/cm, Zanatta et al., have declared method accuracy at 5% level. The data obtained indicate that in sample A_1 the estimated content of phases is approximately 73% rutile and 27% of anatase. In sample A_2, the estimated rutile and anatase content was approximately 38% and 62%, respectively.

EDS measurements showed that the surface of A_2 has a higher amount of oxygen atoms (Table 4) which indicates the higher content of oxides on this surface.

Photocatalytic properties of surfaces

The photocatalytic activity of surfaces was studied in the degradation reaction of MB aqueous solution. The reaction was carried out under weak acidic conditions (pH = 6) and air conditions. The Fig. 5a presents the MB decay in photocatalytic and control processes. The photodegradation rate constant (k_{app}) was determined for each degradation system with the assumption that the ongoing reactions were of the first order from Eq. (3)[47] (Fig. 5b):

$$ln\frac{C_t}{C_0} = -k_{app}t \tag{3}$$

where k_{app} is the apparent rate constant; C_0 and C_t are the initial concentration and concentration at time t.

The degradation rate constants are summarised in Table 5. The A_2 sample exhibited the best catalytic degradation (k_{app} = 0.0267/min). Slightly lower degradation rate was observed for the A_1 sample (k_{app} = 0.0162/min). The degradation rate of MB on A_3 and A_4 surface was 0.0081 and 0.0059/min, respectively. The better photocatalytic activity of A_1 and A_2 is caused by the presence of an oxide layer on the surface. Surface A_1 was characterized by greater roughness than surface A_2 (see S_{dr} parameter Table 2). The higher k_{app} of MB degradation on the A_2 surface indicates that roughness did not influence the photocatalytic efficiency.

Sample	Ti [% at]	O [% at]
A_1	57.9 ± 1.8	42.1 ± 1.8
A_2	53.3 ± 5.1	46.7 ± 5.1

Table 4. The elemental composition of A_1 and A_2 outmost layer.

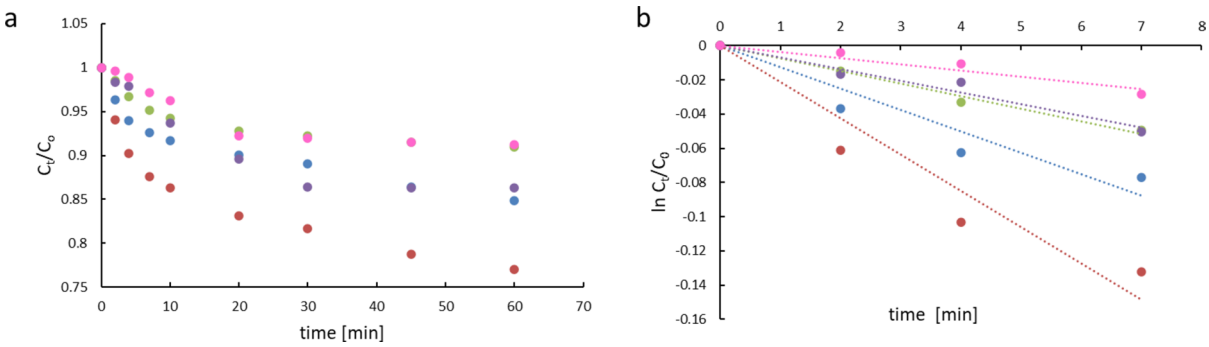

Figure 5. First-order plot of the relative concentrations (C_t/C_0) *vs* time of MB solution (**a**) on surfaces A_1 (blue), A_2 (red), A_3 (green). A_4 (violet). control (MB photolysis. pink); the dependence of ln(C_t/C_0) on time (**b**) A_1 (blue). A_2 (red). A_3 (green). A_4 (violet). control (MB photolysis, pink).

	$k_{app} \times 10^{-3}$[/min]	$t_{1/2}$ [min]
A_1	12.5	113.14
A_2	21.2	66.71
A_3 (LIPSS)	7.4	191.11
A_4 (polished)	6.9	204.96
Control (MB photolysis)	3.6	392.84

Table 5. The degradation kinetic parameters.

The photocatalytic effect of surfaces was observed only for A_1 and A_2. It is involved with the oxide layer of these surfaces. The activated by the light irradiation oxide layer can generate a reactive form as follows:

$$TiO_x \rightarrow^{h\nu} TiO_x\left(e^-, h^+\right)$$

$$O_2 + e^- \rightarrow O_2^{\bullet -}$$

$$H_2O + h^+ \rightarrow H^+ + {}^{\bullet}OH$$

The better photocatalytic activity of A_2 than A_1 may be associated with its phase composition (A_2 has a higher content of anatase, whereas A_1 possesses a greater amount of rutile). It is generally accepted that anatase exhibits higher photocatalytic activity compared to rutile[48]. The TiO_2 band gap is larger than 3 eV (~ 3.0 for rutile and ~ 3.2 for anatase), but anatase exhibits an indirect band gap that is smaller than the direct band gap. In the case of rutile, the size of its indirect bandgap is very similar to that of its direct bandgap. Indirect band-gap semiconductors generally have a longer charge carrier life in comparison to direct band gap materials. The longer lifetime of the electron–hole pair in anatase than in rutile increases the probability of charge carriers participating in surface reactions[49].

Surfaces A_1 and A_2 showed higher photocatalytic activity than microtextured titanium surfaces (Ti grade 2) obtained by Dikici et al.[50] by sandblasting, acid-etching, and anodising. Titanium surfaces were anodised (A), acid-etched and anodised (EA), sandblasted/anodised (SA), and sandblasted/acid-etched/anodised (SEA). The photocatalytic activity of the samples was determined in the degradation reaction of aqueous MB solutions under UV light. The apparent rate constant value increased in order A < EA < SA < SEA (5.2×10^{-3}–6.5×10^{-3}/min) according to the increase in the titanium oxide content on the surface. Fox et al.[51] presented in their article a single-step method of creating porous photocatalytic surfaces via direct laser interference patterning (DLIP) of a titanium substrate (Ti grade 4) by picosecond laser. The photocatalytic activity of the surfaces produced was studied by degradation of MB under ultraviolet–visible (UV-A) light. The value of the apparent kinetic constant of the linear patters for the accumulated fluence in the range of 100–1000 J/cm^2 varies in 1.017×10^{-3}–6.12×10^{-3}/min. The lower pulse energies used in the current studies, compared to those of Fox et al.[51], promoted the formation of a stable oxide layer on the surface, which resulted in better photocatalysis efficiency.

Bacterial adhesion on surfaces

The adhesion of bacteria to the surface, beginning with a loose association of the microorganism to a surface, subsequently converts to strong adhesion. At the final stage of adhesion, bacteria interact with the surface through Lifshitz-van der Waals attractive forces[52]. The adhesion of *Escherichia coli* to various structured Ti disc surfaces was evaluated using the spread plate method in which the number of colony-forming units (CFU) is calculated. A decrease in the number of bacteria cells was observed for the A_1, A_2, and A_3 discs, compared to the unstructured Ti disc, A_4 (Fig. 6A). For each of the modified Ti discs, a reduction in cell population (range between 79 and 87%) was observed. Based on quantitative analysis, disc A_3 showed the highest percentage reduction (87%) in bacterial adhesion. That means the A_3 surface pattern is not conducive to bacterial adhesion.. The adhesion ability to the modified surface of the titanium discs was also assessed through SEM analysis (Fig. 6B). Bacteria colonisation was observed on A_4, while on the remaining samples, the number of cells was small. Bacterial adhesion to the surface depends on both bacterial factors and surface properties. *E. coli* has rod-shaped cells with a diameter of approximately 0.5 µm and a length of approximately 2 µm[53]. *E. coli* is a Gram-negative bacteria, of which the cell wall is composed of a thin layer of peptidoglycan and an outer membrane containing oligosaccharides, which gives the hydrophilic surface of it.. Surfaces A_1 and A_2 contain an oxide layer, which causes them to have a surface charge in aqueous solution. Because surface A_1 has a lower oxygen content than surface A_2, there are fewer active sites where Gram-negative bacteria can bind. Hemmatian et al.[54] reported that the substrate's wettability appeared to be the primary factor influencing the cell adhesion, where the hydrophilic surface resulted in considerably higher adhesion. Regarding the topography of the material, it was found that characteristics related to the size, shape, and distribution of the roughness patterns affect both the attachment and the formation of biofilms of different bacterial strains on various substrates. In addition, topographies on the nanoscale may have bactericidal effects[55]. Here, the different surface textures with and without nanosized structures reduce the adhesion of *E. coli* to the surfaces. The irregular particles on the surface of A_1 reduce the adhesion forces, whereas A_4 increases (Fig. 6C). A surface with a brush morphology, formed by single spikes on the material's surface, can pierce bacterial cells and inhibit their motility, thus ensuring a strong bactericidal

A

Ti disc	Percentage of reduction [%]
A_1	79.4±4.9
A_2	78.8±0.1
A_3	86.9±1.9

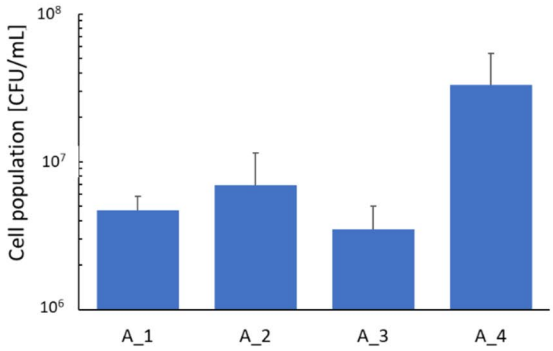

B

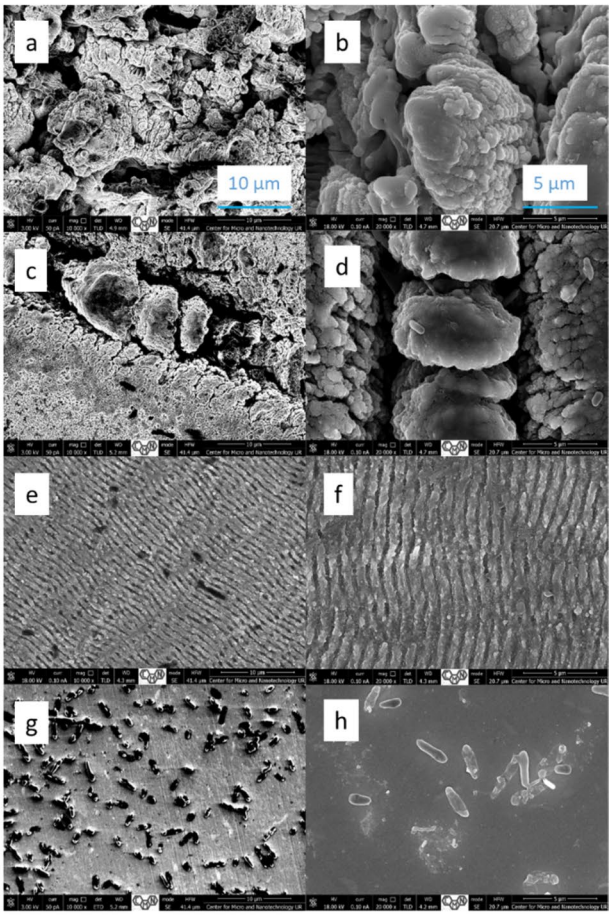

C

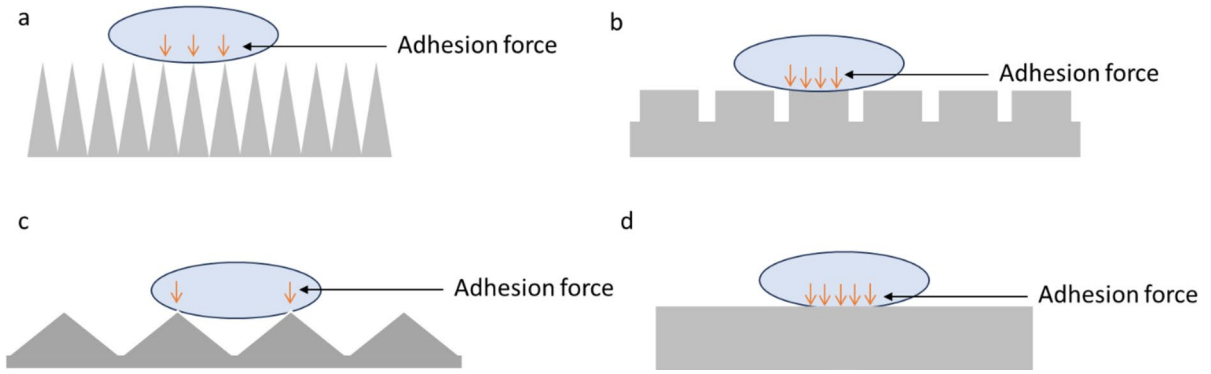

Figure 6. (**A**) The antibacterial activity of various titanium discs is shown as the number of CFU and percentage reduction in the cell population. The error bars indicated the standard deviation of two independent experiments, the statistical analysis was performed with Dunett´s multiple comparison test with GraphPad Prism. (**B**) SEM images of E. coli bacteria cells on surfaces A_1 (a), A_2 (c), A_3 (e), A_4 (g) (before Au spraying), A_1 (b), A_2 (d), A_3 (f), A_4 (h) (after Au spraying). (**C**) Schematic diagram of the bacteria-surface interaction—A_1 (a), A_2 (b), A_3 (c), A_4 (d) [prepared on the basis[58–60]].

effect[56]. However, the observed low number of bacteria on the surface of sample A_1 was the result of difficult adhesion of bacteria to the surface rather than the morphological features of the surface. Typically, bacteria attach to surface structures of submicrometric size, and if the size of the bacteria is much larger compared to the gap between adjacent nanoripples, adhesion is difficult. The results obtained are in agreement with the previous study[57]. Hence, interrupting the initial process of bacterial attachment to the surface is essential to effectively prevent biofilm problems. Therefore, these findings may indicate that surface treatments could be beneficial in the prevention of colonisation of implant surfaces.

Conclusion

Femtosecond-laser processing of Ti surfaces is a convenient single-step process of surface texturing that enables the generation of various patterns depending on used laser parameters. Depending on the laser parameters, the obtained structures differ in roughness, wettability, chemical composition, photocatalytic activity, and antibacterial properties. Modification of the surface with a femtosecond laser with pulse energy values of 4 and 8 mJ promotes the formation of titanium oxides on the surface. Surfaces containing an oxide layer showed photocatalytic activity. The LIPSS structures showed excellent properties in inhibiting *E. coli* adhesion. However, the remaining structures also have very good antimicrobial properties and additionally demonstrate photocatalytic activity.

The results indicated that laser texturing can be an effective method for enhancing implant surfaces and reducing the risks of implant-associated infections.

Data availability

The authors declare that the data supporting the findings of this study are available within the paper. Should any raw data files be needed in another format they are available from the corresponding author upon reasonable request.

Received: 14 May 2024; Accepted: 13 August 2024
Published online: 09 September 2024

References

1. Brunette, D. M., Tenvall, P., Textor, M. & Thomsen, P. *Titanium in Medicine* (Springer, 2001).
2. Özcan, M. & Hämmerle, C. H. Titanium as a reconstruction and implant material in dentistry: Advantages and pitfalls. *Materials* **5**, 1528–1545. https://doi.org/10.3390/ma5091528 (2012).
3. Albrektsson, T. & Wennerberg, A. On osseointegration in relation to implant surfaces. *Clin. Implant. Dent. Rel. Res.* **21**, 4–7. https://doi.org/10.1111/cid.12742 (2019).
4. Kim, J. C., Lee, M. & Yeo, I. S. L. Three interfaces of the dental implant system and their clinical effects on hard and soft tissues. *Mater. Horiz.* **9**, 1387–1411. https://doi.org/10.1039/D1MH01621K (2022).
5. Sasada, Y. & Cochran, D. L. Implant-abutment connections: A review of biologic consequences and peri-implantitis implications. *Int. J. Oral. Maxillofac. Implants.* **32**(6), 1296–1307. https://doi.org/10.11607/jomi.5732 (2017).
6. Wang, Y., Zhang, Y. & Miron, R. J. Health, maintenance, and recovery of soft tissues around implants. *Clin. Implant. Dent. Relat. Res.* **18**(3), 618–634. https://doi.org/10.1111/cid.12343 (2016).
7. Busscher, H. J. *et al.* Biomaterial-associated infection: Locating the finish line in the race for the surface. *Sci. Transl. Med.* **4**, 153–200. https://doi.org/10.1126/scitranslmed.3004528 (2012).
8. Kunrath, M. F., Monteiro, M. S., Gupta, S., Hubler, R. & de Oliveira, S. D. Influence of titanium and zirconia modified surfaces for rapid healing on adhesion and biofilm formation of *Staphylococcus* epidermidis. *Arch. Oral Biol.* **117**, 104824. https://doi.org/10.1016/j.archoralbio.2020.104824 (2020).
9. Bermejo, P. *et al.* Biofilm formation on dental implants with different surface micro-topography: An in vitro study. *Clin. Oral Implants Res.* **30**(8), 725–734. https://doi.org/10.1111/clr.13455 (2019).
10. Kunrath, M. F. & Gerhardt, M. D. N. Trans-mucosal platforms for dental implants: Strategies to induce muco-integration and shield peri-implant diseases. *Dent. Mater.* **39**(9), 846–859. https://doi.org/10.1016/j.dental.2023.07.009 (2023).
11. Kunrath, M. F., Muradás, T. C., Penha, N. & Campos, M. M. Innovative surfaces and alloys for dental implants: What about biointerface-safety concerns?. *Dent. Mater.* **37**(10), 1447–1462. https://doi.org/10.1016/j.dental.2021.08.008 (2021).
12. Chen, Z. *et al.* Nanotopography-based strategy for the precise manipulation of osteoimmunomodulation in bone regeneration. *Nanoscale* **9**, 18129–18152. https://doi.org/10.1039/C7NR05913B (2017).
13. Souza, J. C. M. *et al.* Nano-scale modification of titanium implant surfaces to enhance osseointegration. *Acta Biomater.* **94**, 112–131. https://doi.org/10.1016/j.actbio.2019.05.045 (2019).
14. Seo, Y. *et al.* Femtosecond laser induced nano-textured micropatterning to regulate cell functions on implanted biomaterials. *Acta Biomater.* **116**, 138–148. https://doi.org/10.1016/j.actbio.2020.08.044 (2020).
15. Orazi, L., Pelaccia, R., Mishchenko, O., Reggiani, B. & Pogorielov, M. Fast LIPSS based texturing process of dental implants with complex geometries. *CIRP Ann.-Manuf. Techn.* **69**, 233–236. https://doi.org/10.1016/j.cirp.2020.04.065 (2020).
16. Nakajima, A., Omiya, M. & Jiwang, Y. J. Generation of micro/nano hybrid surface structures on copper by femtosecond pulsed laser irradiation. *Nanomanuf. Metrol.* **5**, 274–282. https://doi.org/10.1007/s41871-022-00135-9 (2022).
17. Kirner, S. V. *et al.* Mimicking bug-like surface structures and their fluid transport produced by ultrashort laser pulse irradiation of steel. *Appl. Phys. A.* **123**, 754. https://doi.org/10.1007/s00339-017-1317-3 (2017).
18. Kisała, J. *et al.* Synthesis of micro-spikes and herringbones structures by femtosecond laser pulses on a titanium plate—a new material for water organic pollutants degradation. *Materials* **14**(19), 5556. https://doi.org/10.3390/ma14195556 (2021).
19. Costa, R. C. *et al.* Fitting pieces into the puzzle: The impact of titanium-based dental implant surface modifications on bacterial accumulation and polymicrobial infections. *Adv. Colloid Interface Sci.* **298**, 102551. https://doi.org/10.1016/j.cis.2021.102551 (2021).
20. Komorowski, P. *et al.* Designing laser-modified Surface structures on titanium alloy custom medical implants using a hybrid manufacturing technology. *J. Biomed. Mater. Res. B Appl. Biomater.* **108**, 1790–1800. https://doi.org/10.1002/jbm.b.34521 (2020).
21. Luo, X. *et al.* Biocompatible nano-ripples structured surfaces induced by femtosecond laser to rebel bacterial colonization and biofilm formation. *Opt. Laser Technol.* **124**, 105973. https://doi.org/10.1016/j.optlastec.2019.105973 (2020).
22. Eghbali, N., Naffakh-Moosavy, H., Sadeghi Mohammadi, S. & Naderi-Manesh, H. The influence of laser frequency and groove distance on cell adhesion, cell viability, and antibacterial characteristic of Ti-6Al-4V dental implants treated by modern fiber engraving laser. *Dent. Mater.* **37**, 547–558. https://doi.org/10.1016/j.dental.2020.12.007 (2021).
23. Papa, S. *et al.* Dual-functionalized titanium by ultrafast laser texturing to enhance human gingival fibroblasts adhesion and minimize *Porphyromonas gingivalis* colonization. *Appl. Surf. Sci.* **606**, 154784. https://doi.org/10.1016/j.apsusc.2022.154784 (2022).
24. Meinshausen, A.-K. *et al.* Aspect ratio of nano/microstructures determines *Staphylococcus aureus* adhesion on PET and titanium surfaces. *J. Appl. Microbiol.* **131**, 1498–1514. https://doi.org/10.1111/jam.15033 (2021).
25. Choi, J. Y. *et al.* Influence of nanocoated calcium phosphate on two different types of implant surfaces in different bone environment: An animal study. *Clin. Oral Implants Res.* **24**(9), 1018–1022. https://doi.org/10.1111/j.1600-0501.2012.02492.x (2013).
26. Vorobyev, A. Y. & Guo, C. Direct femtosecond laser surface nano/microstructuring and its applications. *Laser Photon. Rev.* **7**(3), 385–407. https://doi.org/10.1002/lpor.201200017 (2013).
27. Lausmaa, J. *Mechanical, Thermal, Chemical and Electrochemical Surface Treatment of Titanium. Titanium in Medicine, Engineering Materials* (Springer, 2001). https://doi.org/10.1007/978-3-642-56486-4_8.

28. Bonse, J., Höhm, S., Kirner, S. V., Rosenfeld, A. & Krüger, J. Laser-induced periodic surface structures—a scientific evergreen. *IEEE J. Sel. Top. Quant. Electron.* **23**, 9000615. https://doi.org/10.1109/JSTQE.2016.2614183 (2017).
29. Bonse, J. Quo vadis LIPSS?—Recent and future trends on laser-induced periodic surface structures. *Nanomaterials* **10**, 1950. https://doi.org/10.3390/nano10101950 (2020).
30. Zhang, X., Wang, L. & Levänen, E. Superhydrophobic surfaces for the reduction of bacterial adhesion. *RSC Adv.* **3**, 12003–12020. https://doi.org/10.1039/C3RA40497H (2013).
31. Liu, L., Shi, H., Yu, H., Yan, S. & Luan, S. The recent advances in surface antibacterial strategies for biomedical catheters. *Biomater. Sci.* **8**, 4095–4108. https://doi.org/10.1039/D0BM00659A (2020).
32. Liang, X. J. *et al.* Effect of superhydrophobic surface of titanium on *Staphylococcus aureus* adhesion. *J. Nanomater.* **2011**, 178921. https://doi.org/10.1155/2011/178921 (2011).
33. Ashok, D. *et al.* Superhydrophobic surfaces to combat bacterial surface colonization. *Adv. Mater. Interfaces* **10**, 2300324. https://doi.org/10.1002/admi.202300324 (2023).
34. Jothi Prakash, C. G. & Prasanth, R. Approaches to design a surface with tunable wettability: A review on surface properties. *J. Mater. Sci.* **56**, 108–135. https://doi.org/10.1007/s10853-020-05116-1 (2021).
35. Singh, A. V. *et al.* Bottom-up engineering of the surface roughness of nanostructured cubic zirconia to control cell adhesion. *Nanotechnology* **23**(47), 475101. https://doi.org/10.1088/0957-4484/23/47/475101 (2012).
36. Amani, H. *et al.* Controlling cell behavior through the design of biomaterial surfaces: A focus on surface modification techniques. *Adv. Mater. Interfaces.* **6**, 1900572. https://doi.org/10.1002/admi.201900572 (2019).
37. Yang, W., Yu, H., Li, G., Wang, Y. & Liu, L. Facile modulation of cell adhesion to a poly(ethylene glycol) diacrylate film with incorporation of polystyrene nano-spheres. *Biomed. Microdev.* **18**(6), 107. https://doi.org/10.1007/s10544-016-0133-4 (2016).
38. Shalabi, M. M., Gortemaker, A., Van't Hof, M. A., Jansen, J. A. & Creugers, N. H. Implant surface roughness and bone healing: A systematic review. *J. Dent. Res.* **85**(6), 496–500. https://doi.org/10.1177/154405910608500603 (2006).
39. Chung, T. W., Liu, D. Z., Wang, S. Y. & Wang, S. S. Enhancement of the growth of human endothelial cells by surface roughness at nanometer scale. *Biomaterials* **24**(25), 4655–4661. https://doi.org/10.1016/s0142-9612(03)00361-2 (2003).
40. Kabekkodu, S. PDF-4+ (Database). International Centre for Diffraction Data: Newtown Square, PA, USA (2015).
41. Crystallography Open Database. http://www.crystallography.net/cod/. Accessed 5 Sep 2021.
42. Ivanov, S. *et al.* Synthesis, characterization, and photocatalytic properties of sulfur- and carbon-codoped TiO_2 nanoparticles. *Nanoscale Res. Lett.* **11**, 140. https://doi.org/10.1186/s11671-016-1353-5 (2016).
43. Challagulla, S., Tarafder, K., Ganesan, R. & Roy, S. Structure sensitive photocatalytic reduction of nitroarenes over TiO_2. *Sci. Rep.* **7**(1), 8783. https://doi.org/10.1038/s41598-017-08599-2 (2017).
44. Liu, G. *et al.* Titania polymorphs derived from crystalline titanium diboride. *Cryst. Eng. Comm.* **11**, 2677–2682. https://doi.org/10.1039/B909191M (2009).
45. Zanatta, A. A fast-reliable methodology to estimate the concentration of rutile or anatase phases of TiO_2. *AIP Adv.* **7**, 075201. https://doi.org/10.1063/1.4992130 (2017).
46. Jasinski, J. J. *et al.* Qualitative and semi-quantitative phase analysis of TiO2 thin layers by Raman imaging. *J. Mol. Struct.* **1260**, 132803. https://doi.org/10.1016/j.molstruc.2022.132803 (2022).
47. Atkins, P. & De Paula, J. *Atkins' Physical Chemistry* (W. H. Freeman and Company, 2006).
48. Liu, L., Zhao, H., Andino, J. M. & Li, Y. Photocatalytic CO_2 reduction with H_2O on TiO_2 nanocrystals: Comparison of anatase, rutile and brookite polymorphs and exploration of surface chemistry. *ACS Catal.* **2**, 1817–1828. https://doi.org/10.1021/cs300273q (2012).
49. Luttrell, T. *et al.* Why is anatase a better photocatalyst than rutile? Model studies on epitaxial TiO_2 films. *Sci. Rep.* **4**, 4043. https://doi.org/10.1038/srep04043 (2014).
50. Dikici, T., Demirci, S. & Erol, M. Enhanced photocatalytic activity of micro/nano textured TiO_2 surfaces prepared by sandblasting/acid-etching/anodizing process. *J. Alloys Compd.* **694**, 246–252. https://doi.org/10.1016/j.jallcom.2016.09.330 (2017).
51. Fox, T. *et al.* Single-step production of photocatalytic surfaces via direct laser interference patterning of titanium. *ChemNanoMat* **9**, e202300314. https://doi.org/10.1002/cnma.202300314 (2023).
52. Carniello, V., Peterson, B. W., van der Mei, H. C. & Busscher, H. J. Physico-chemistry from initial bacterial adhesion to surface-programmed biofilm growth. *Adv. Colloid Interface Sci.* **261**, 1–14. https://doi.org/10.1016/j.cis.2018.10.005 (2018).
53. Iyer, D., Laws, E. & LaJeunesse, D. *Escherichia coli* adhesion and biofilm formation on polymeric nanostructured surfaces. *ACS Omega* **8**(50), 47520–47529. https://doi.org/10.1021/acsomega.3c04747 (2023).
54. Hemmatian, T., Lee, H. & Kim, J. Bacteria adhesion of textiles influenced by wettability and pore characteristics of fibrous substrates. *Polym. (Basel)* **13**(2), 223. https://doi.org/10.3390/polym13020223 (2021).
55. Kreve, S. & Reis, A. C. D. Bacterial adhesion to biomaterials: What regulates this attachment? A review. *Jpn. Dent. Sci. Rev.* **57**, 85–96. https://doi.org/10.1016/j.jdsr.2021.05.003 (2021).
56. Diu, T. *et al.* Cicada-inspired cell-instructive nanopatterned arrays. *Sci. Rep.* **4**, 7122. https://doi.org/10.1038/srep07122 (2014).
57. Nikam, M. *et al.* Influence of micro-textures on wettability and antibacterial behavior of Titanium surfaces against *S. aureus* and *E. coli*: In vitro studies. *Int. J. Interact. Des. Manuf.* https://doi.org/10.1007/s12008-023-01287-8 (2023).
58. Lai, C. Q. Bacterial attachment, aggregation, and alignment on subcellular nanogratings. *Langmuir* **34**(13), 4059–4070. https://doi.org/10.1021/acs.langmuir.8b00350 (2018).
59. Shin, D. & Meredith, J. C. Influence of topography on adhesion and bioadhesion. In *Contamination Mitigating Polymeric Coatings for Extreme Environments. Advances in Polymer Science* (eds Wohl, C. & Berry, D.) (Springer, 2018). https://doi.org/10.1007/12_2017_40.
60. Spengler, C. *et al.* Strength of bacterial adhesion on nanostructured surfaces quantified by substrate morphometry. *Nanoscale* **11**, 19713–19722. https://doi.org/10.1039/C9NR04375F (2019).

Author contributions

A. B. contributed to investigation, methodology, writing original draft, writing – review & editing; R. W.-N. contributed to Raman measurements, data interpretation; M. K.-L. contributed to investigation – antibacterial properties test, writing original draft; P. K. contributed to roughness and SEM measurements; D. P. contributed to SEM measurements, B. C. contributed to XRD measurements; Y. B. contributed to Ti surfaces structurization, writing the original draft; J. K. contributed to conceptualisation, methodology, investigation, writing original draft, writing – review & editing, supervision.

Funding

The authors received no financial support for the research, authorship, and/or publication of this article.

Competing interests

The authors declare no competing interests.

Additional information

Correspondence and requests for materials should be addressed to A.B. or J.K.

Reprints and permissions information is available at www.nature.com/reprints.